Supplementary information for "Estimating charge-transport properties of fuel-cell and electrolyzer catalyst layers via electrochemical impedance spectroscopy"*

A. Kosakian[a,b], M. Secanell[a,*]

[a] *Energy Systems Design Laboratory, Department of Mechanical Engineering, University of Alberta, Canada*
[b] *Department of Mathematical and Statistical Sciences, University of Alberta, Canada*

1. Effect of current density on the simulated impedance spectra

The spectra simulated numerically at 0.01 and 0.1 A/cm^2, shown in Figures 5 and 6 of the main text, were in a good agreement with equation (17). As expected, the discrepancy between the numerical and analytical spectra increased with current density, as seen in Figures S1 and S2, due to the assumptions made in the derivation of the analytical model.

2. Analytical fits of the homogeneous-catalyst-layer impedance spectra

2.1. H_2/O_2 spectroscopy

The plots of the simulated H_2/O_2 spectra fitted with equations (16) and (18) from the main text are provided in Figures S3 and S4. The extracted resistances and conductivities are given in Tables 4 and 5 of the main text.

Contour plots of the fitting residuals obtained with equation (18) from the main text are shown in Figure S5. The fitted and the exact conductivities are marked with the solid red and the hollow black markers, respectively, and their labels indicate the corresponding residuals. The residual computed with the exact conductivities was higher due to the numerical error in the simulations. In cases I and II, the simulated catalyst layer was highly electronically conductive, and the residual plots contain a range of electronic conductivities with relatively low residual values. Both protonic and electronic conductivities were low in case IV, and each residual graph has a unique optimum point. Two search regions are shown for case V, with region 1 neighboring the conductivities used in the EIS simulation and region 2 neighboring the mirrored conductivities. As expected, the residual plots of the mirrored case V were qualitatively similar to those in case I.

*This is the authors' preprint of the supporting information for the article published in Electrochimica Acta on November 23, 2020 (`https://doi.org/10.1016/j.electacta.2020.137521`). This document does not contain the corrections and improvements made during the review and proof processes. Please cite the published article.

*Corresponding author
Email address: `secanell@ualberta.ca` (M. Secanell)

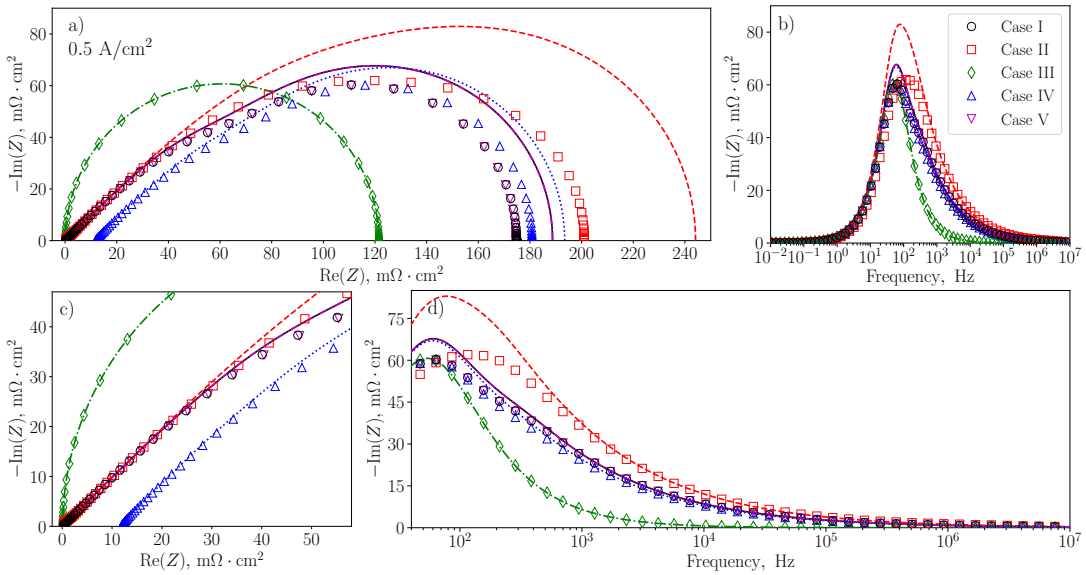

Figure S1: Comparison of the H_2/O_2 spectra simulated numerically (markers) to those computed analytically with equation (17) from the main text (lines) at 0.5 A/cm^2: a), c) Nyquist plot and its high-frequency portion; b), d) Bode plot of the imaginary impedance component and its high-frequency portion. Every twentieth point is shown for clarity.

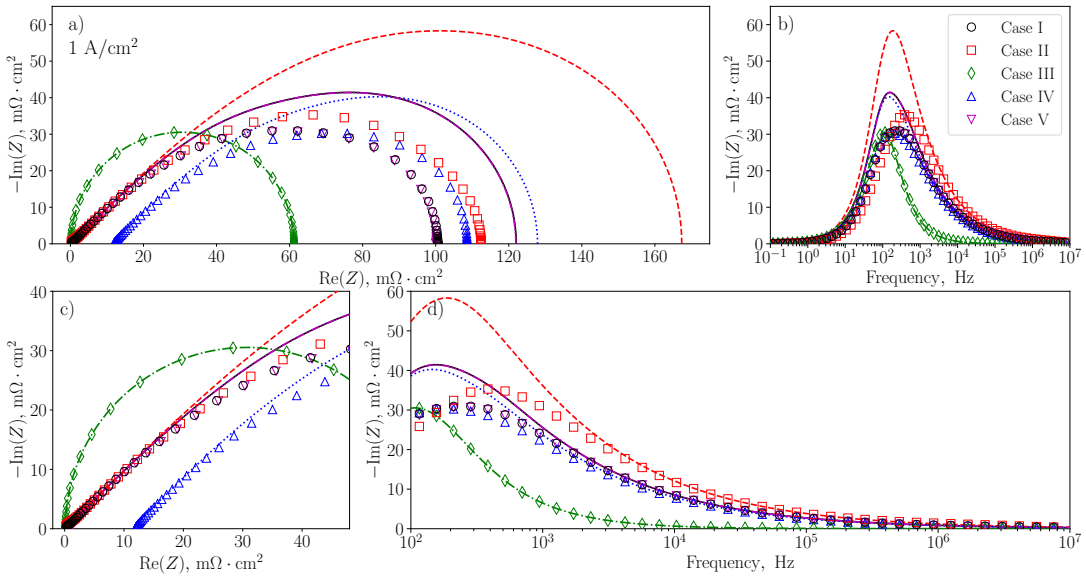

Figure S2: Comparison of the H_2/O_2 spectra simulated numerically (markers) to those computed analytically with equation (17) from the main text (lines) at 1 A/cm^2: a), c) Nyquist plot and its high-frequency portion; b), d) Bode plot of the imaginary impedance component and its high-frequency portion. Every twentieth point is shown for clarity.

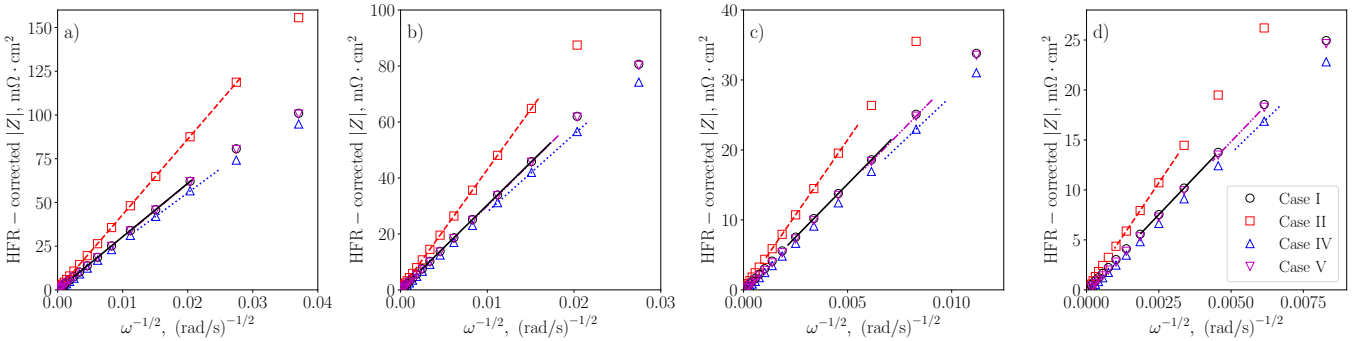

Figure S3: High-frequency portions of the HFR-corrected H_2/O_2 impedance magnitude against $\omega^{-1/2}$ (markers) and their fits obtained with equation (16) from the main text (lines): a) 0.01 A/cm^2; b) 0.1 A/cm^2; c) 0.5 A/cm^2; and d) 1 A/cm^2. Every fortieth data point is shown for clarity.

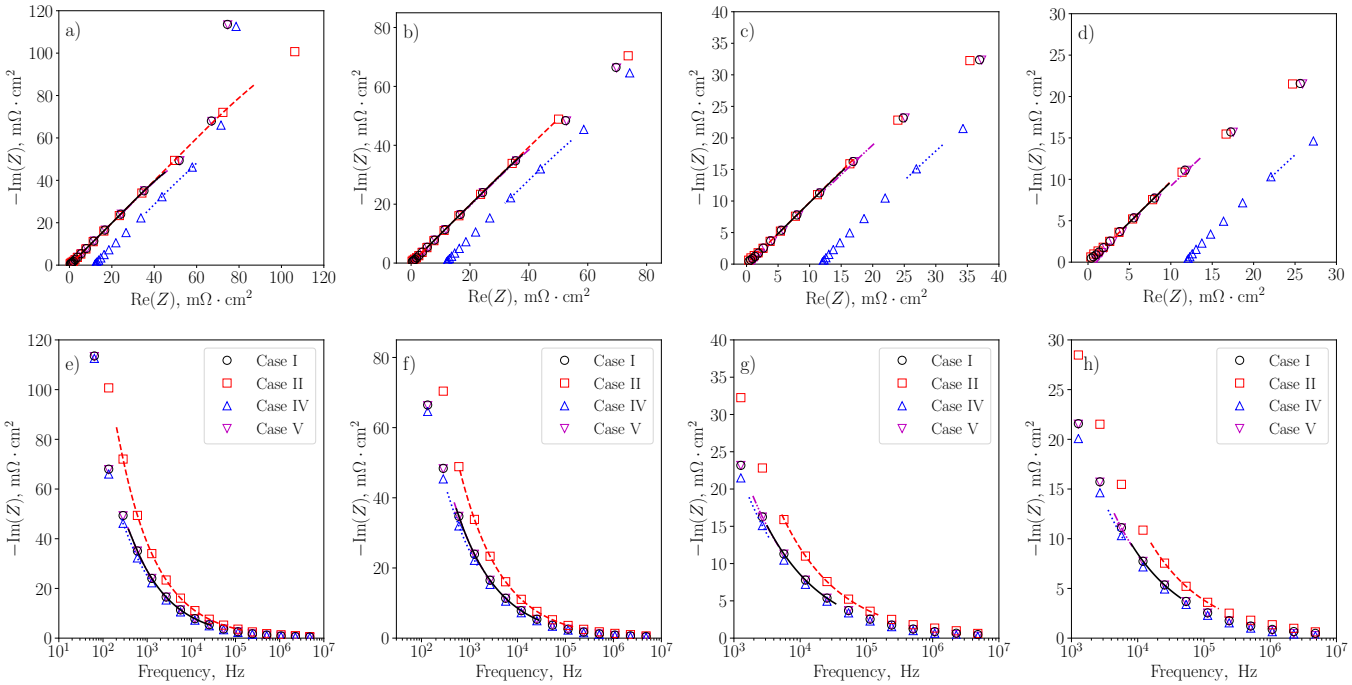

Figure S4: High-frequency portions of the simulated H_2/O_2 spectra (markers) and their fits obtained with equation (18) from the main text (lines): a), e) 0.01 A/cm^2; b), f) 0.1 A/cm^2; c), g) 0.5 A/cm^2; and d), h) 1 A/cm^2. Graphs a)–d) are Nyquist plots; graphs e)–h) are Bode plots of the imaginary impedance component. Every fiftieth data point is shown for clarity.

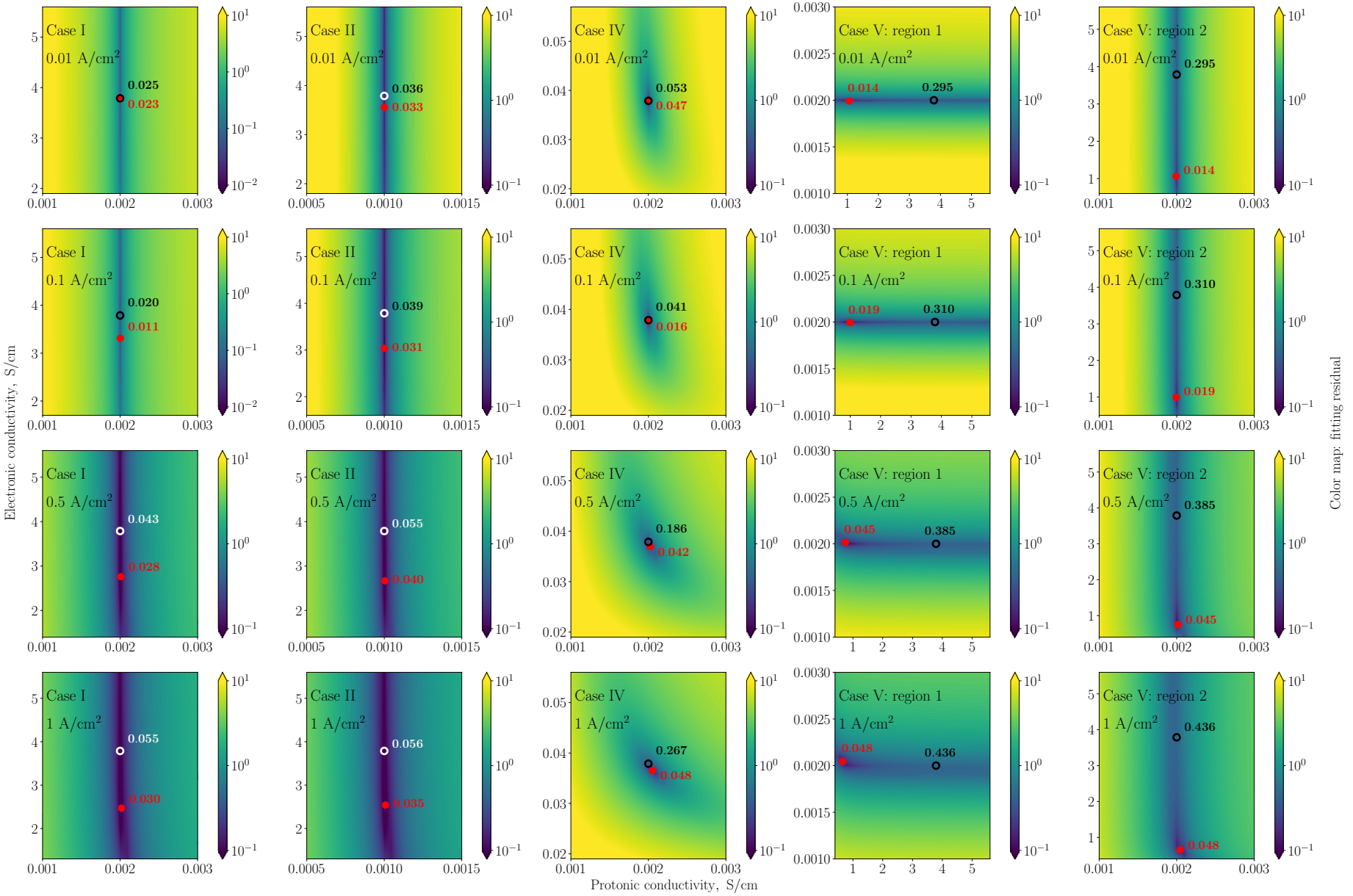

Figure S5: Residual distributions of the fits given in Tables 4 and 5 for equation (18) from the main text. The solid red and the hollow black markers in each graph indicate the fitted and the exact conductivity values, respectively. The corresponding labels provide the residual values between the numerical and the analytical spectra.

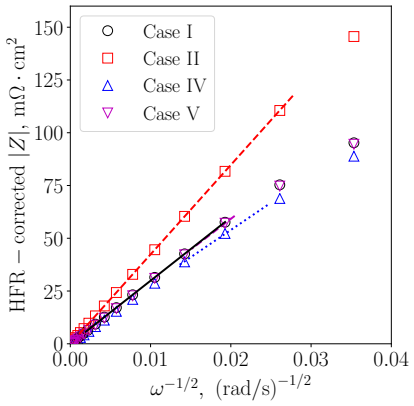

Figure S6: High-frequency portions of the HFR-corrected H_2/N_2 impedance magnitude against $\omega^{-1/2}$ (markers) and their fits obtained with equation (16) (lines). Every fifth data point is shown for clarity.

2.2. H_2/N_2 spectroscopy

The plots of the simulated H_2/N_2 spectra fitted with equations (16), (23), and (25) from the main text are provided in Figures S6 and S7. The extracted resistances and conductivities are given in Table 6 of the main text and Table S1, respectively. Contour plots of the fitting residuals obtained with equation (25) from the main text are shown in Figure S8. As it was the case for equation (18), sensitivity of equation (25) to the dominating conductivity is low.

3. Dependency of the protonic-potential distribution in a homogeneous CL on current density

The dependency of the dimensionless protonic-potential distribution in a homogeneous CL on current density is illustrated in Figure S9. The potential distribution was normalized by the magnitude of the potential drop across the layer.

4. Effect of heterogeneous ionomer loading

4.1. Catalyst layer with high electronic conductivity

Impedance spectra simulated for a catalyst layer with heterogeneous ionomer loading and high electronic conductivity (for case I from Table 3) at 0.1 and 0.5 A/cm^2 are shown in Figures S10 and S11.

4.2. Catalyst layer with low electronic conductivity

The impedance spectra simulated for a catalyst layer with heterogeneous ionomer loading and low electronic conductivity (for case IV from Table 3) were qualitatively similar to those obtained with higher electronic conductivity. The simulated H_2/N_2 spectra are shown in Figure S12. It must be noted that the phase angle reported in this case was computed based on the HFR-corrected spectra to correspond to the slope of the linear branch at high frequencies. When HFR is significant, this phase angle is different from the phase angle of the impedance (i.e., the voltage-current phase shift).

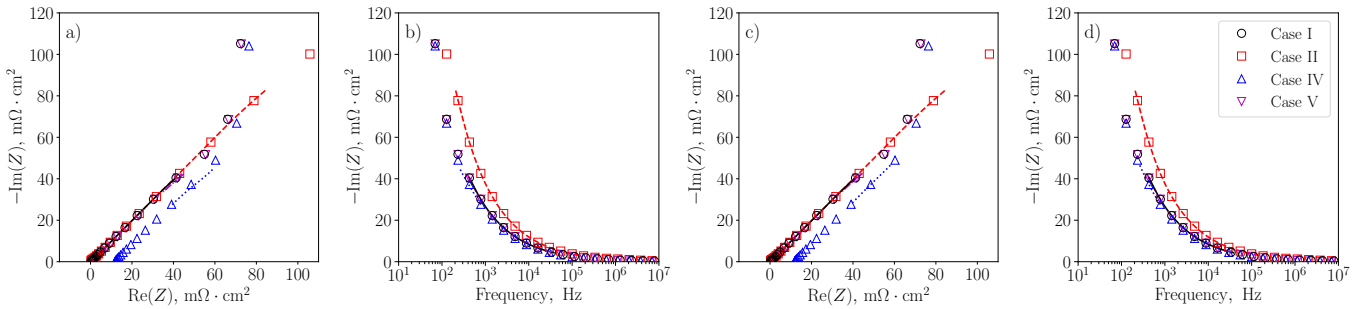

Figure S7: High-frequency portions of the simulated H_2/N_2 spectra and their fits obtained with: a), b) equation (23) and c), d) equation (25). Graphs a) and c) are Nyquist plots; graphs b) and d) are Bode plots of the imaginary impedance component. Every fifth data point is shown for clarity.

Table S1: Catalyst-layer protonic and electronic conductivities fitted to the H_2/N_2 spectra using the two graphical approaches illustrated in Figure 3 and equations (16), (23), and (25) of the main text, along with the exact values. In case of equations (16) and (23), resistance was fitted and then converted into conductivity using equation (21). The modified graphical approach from Figure 3(b) resulted in two equally valid pairs of protonic and electronic conductivities. Two conductivity pairs given in case V for equation (25) resulted in similar, within 10^{-11} m$\Omega \cdot$ cm^2, residuals (conductivity corresponding to the smaller residual is given first).

Case	$\boldsymbol{\sigma^{\mathrm{EKM}}_{\mathrm{H^+}}}$, **mS/cm (Fit, Fig. 3(a))**	$\boldsymbol{\sigma^{\mathrm{K}}_{\mathrm{H^+}}}$, **mS/cm (Fit, Fig. 3(b))**	$\boldsymbol{\sigma^{\mathrm{K}}_{\mathrm{e^-}}}$, **mS/cm (Fit, Fig. 3(b))**	$\boldsymbol{\sigma^{\mathrm{EKM}}_{\mathrm{H^+}}}$, **mS/cm (Fit, Eq. (16))**	$\boldsymbol{\sigma^{\mathrm{EKM}}_{\mathrm{H^+}}}$, **mS/cm (Fit, Eq. (23))**	$\boldsymbol{\sigma^{\mathrm{K}}_{\mathrm{H^+}}}$, **mS/cm (Fit, Eq. (25))**	$\boldsymbol{\sigma^{\mathrm{K}}_{\mathrm{e^-}}}$, **mS/cm (Fit, Eq. (25))**	$\boldsymbol{\sigma^{\mathrm{eff}}_{\mathrm{H^+}}}$, **mS/cm (Model input, Table 3)**	$\boldsymbol{\sigma^{\mathrm{eff}}_{\mathrm{e^-}}}$, **mS/cm (Model input, Table 3)**
I	1.99	1.99, 5526	5526, 1.99	2.06	2.08	2.07	2077	**2.00**	**3788**
II	0.993	0.993, 6707	6707, 0.993	1.03	1.04	1.04	1769	**1.00**	**3788**
IV	1.98	1.98, 38.6	38.6, 1.98	2.77	2.50	2.09	37.9	**2.00**	**37.9**
V	1.95	1.99, 306	306, 1.99	2.18	2.13	2.07, 469	469, 2.07	**3788**	**2.00**

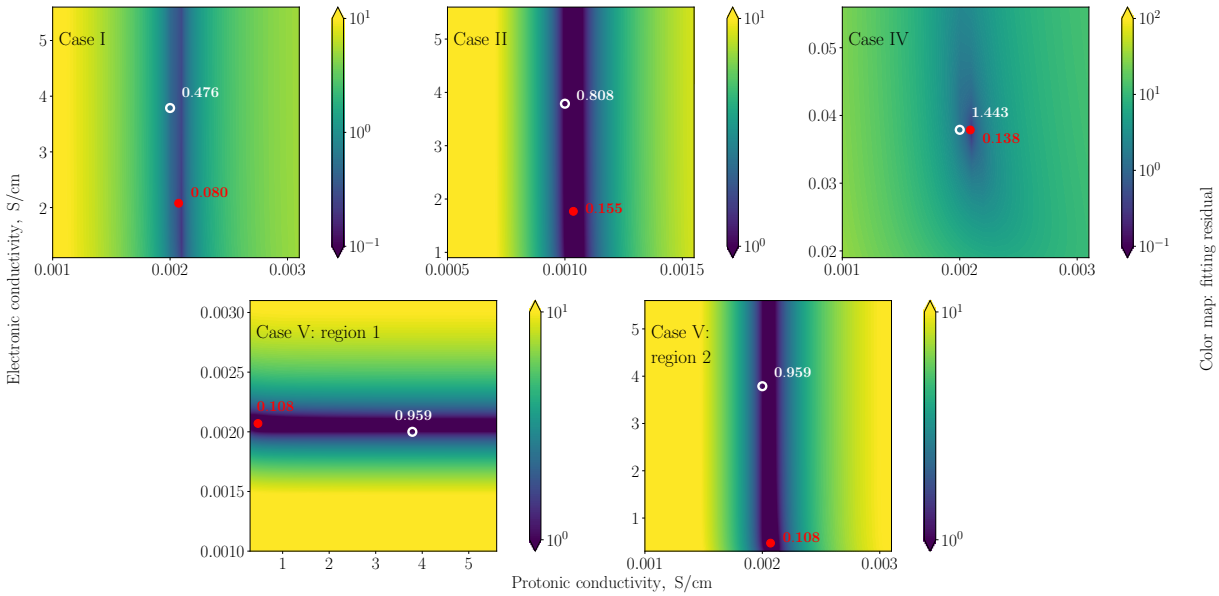

Figure S8: Residual distributions of fits given in Table 6 of the main text and Table S1 for equation (25). The solid red and the hollow white markers in each graph indicate the fitted and the exact conductivity values, respectively. The corresponding labels provide the residual values between the numerical and the analytical spectra.

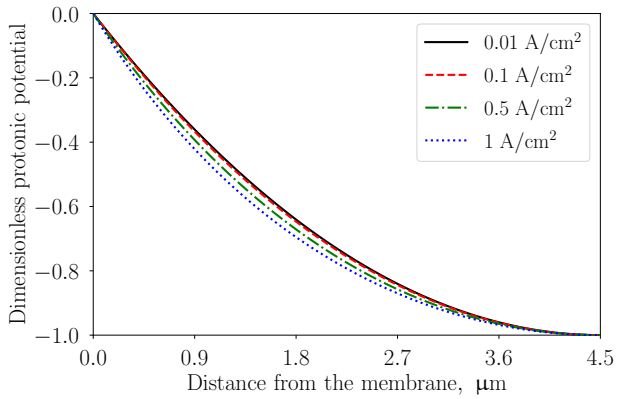

Figure S9: Comparison of the dimensionless protonic-potential distributions in a homogeneous CL (case I).

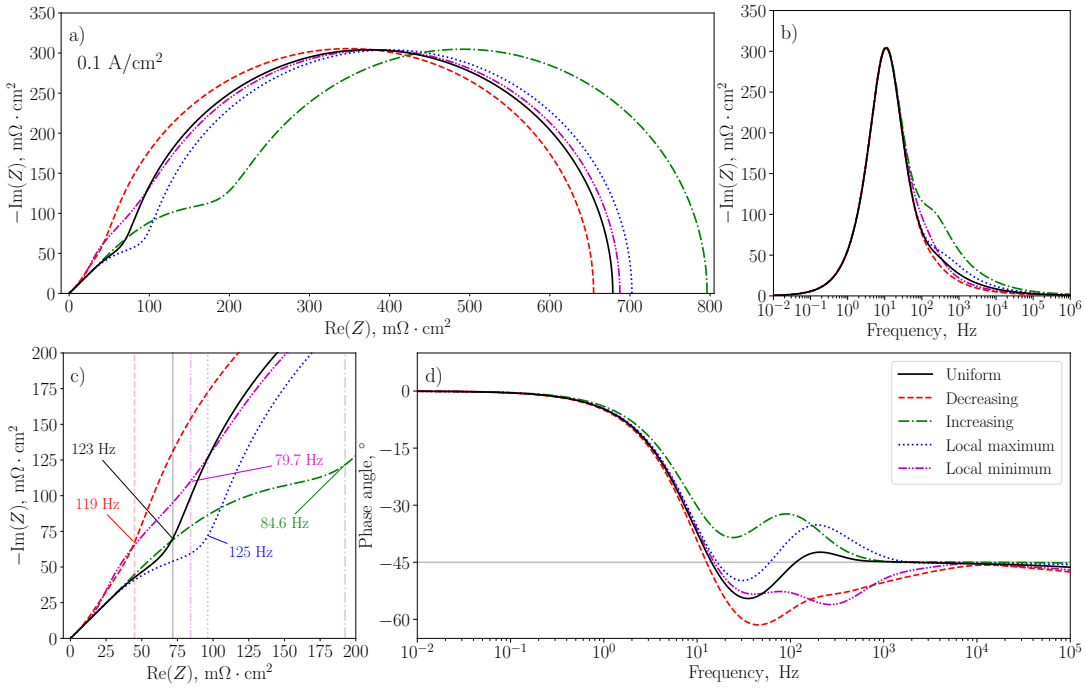

Figure S10: Comparison of the H_2/O_2 spectra simulated numerically for the ionomer-loading distributions from Figure 1 at 0.1 A/cm^2: a), c) Nyquist plot and its high-frequency portion; b), d) Bode plot of the imaginary impedance component and its high-frequency portion. Vertical lines represent the total ohmic resistance computed through ohmic heating (equations (6) and (7)).

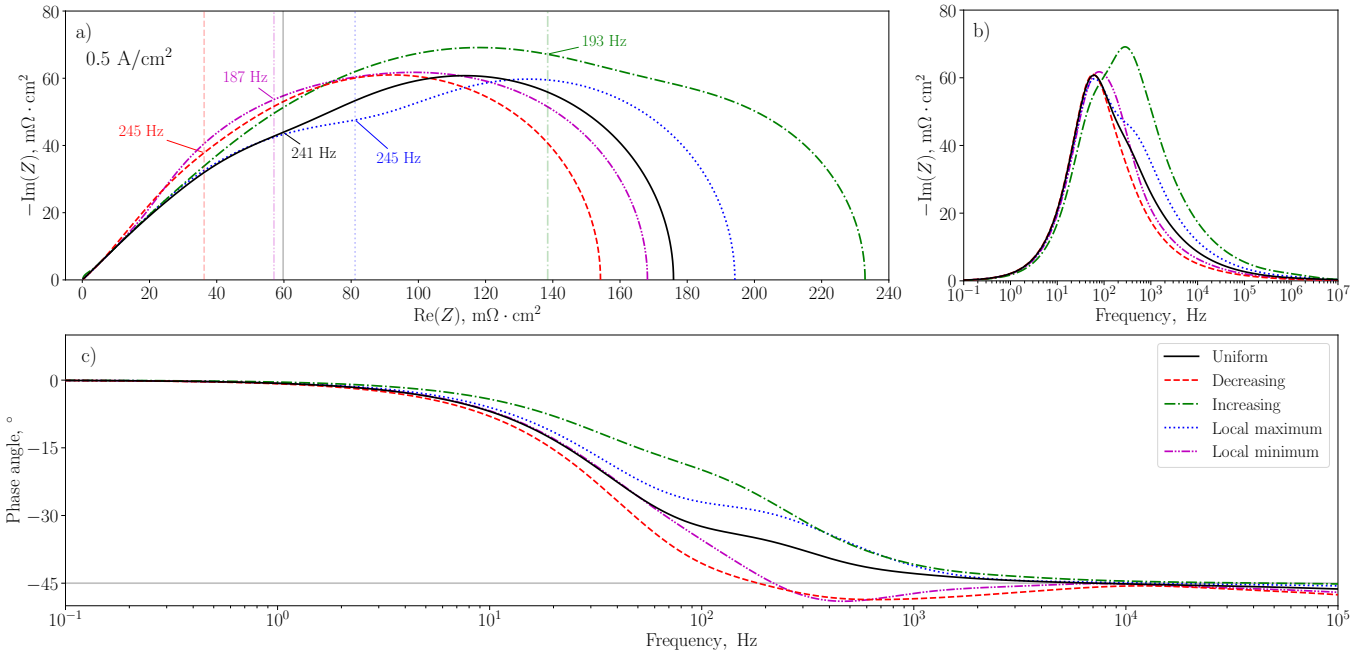

Figure S11: Comparison of the H_2/O_2 spectra simulated numerically for the ionomer-loading distributions from Figure 1 at 0.5 A/cm^2: a) Nyquist plot and b) Bode plot of the imaginary impedance component. Vertical lines represent the total ohmic resistance computed through ohmic heating (equations (6) and (7)).

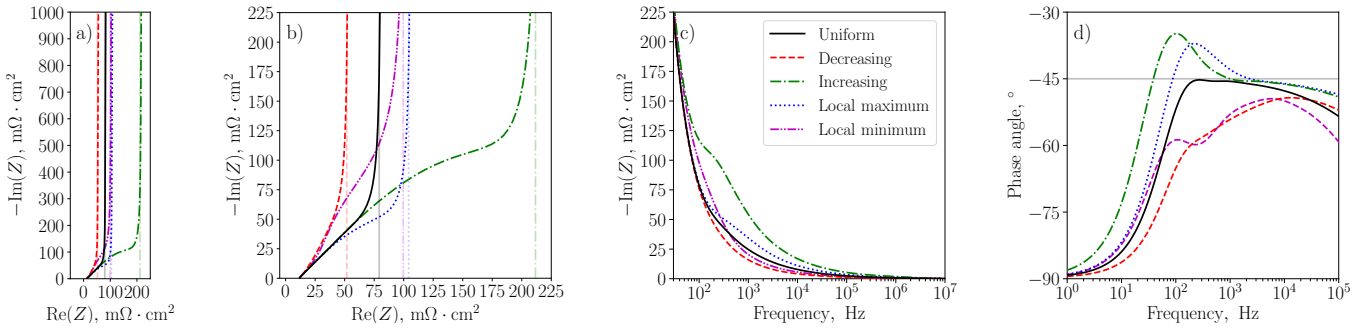

Figure S12: Comparison of the H_2/N_2 spectra simulated numerically for the ionomer-loading distributions from Figure 1 and the low electronic conductivity for case IV from Table 3: a), b) Nyquist plot and its high-frequency portion; c) Bode plot of the imaginary impedance component (high-frequency portion). Vertical lines represent the total ohmic resistance computed through ohmic heating (equations (6) and (7); estimates at 0.1 mA/cm^2 are shown).

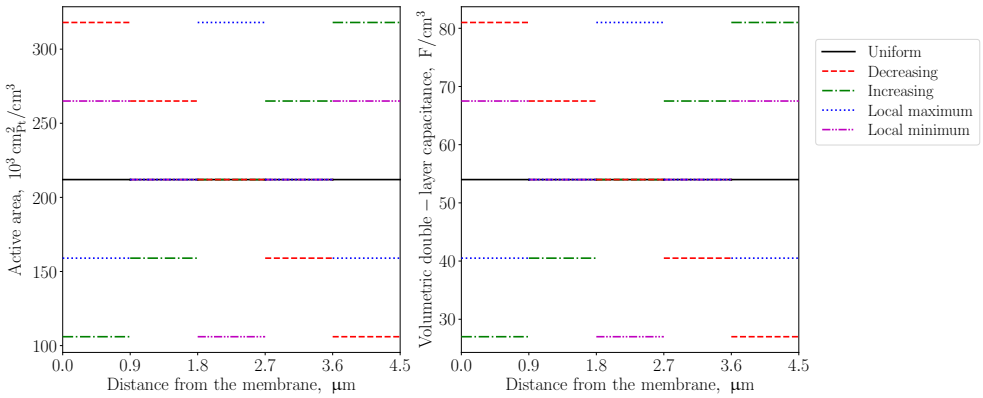

Figure S13: Illustration of the heterogeneous-catalyst-layer property distributions used in this work: a) active area; and b) volumetric double-layer capacitance. The "decreasing", "increasing", and "uniform" distributions coincide at $x \in [1.8,\ 2.7)$ μm; the "local maximum", "local minimum", and "uniform" distributions coincide at $x \in [0.9,\ 1.8) \cup [2.7,\ 3.6)$ μm.

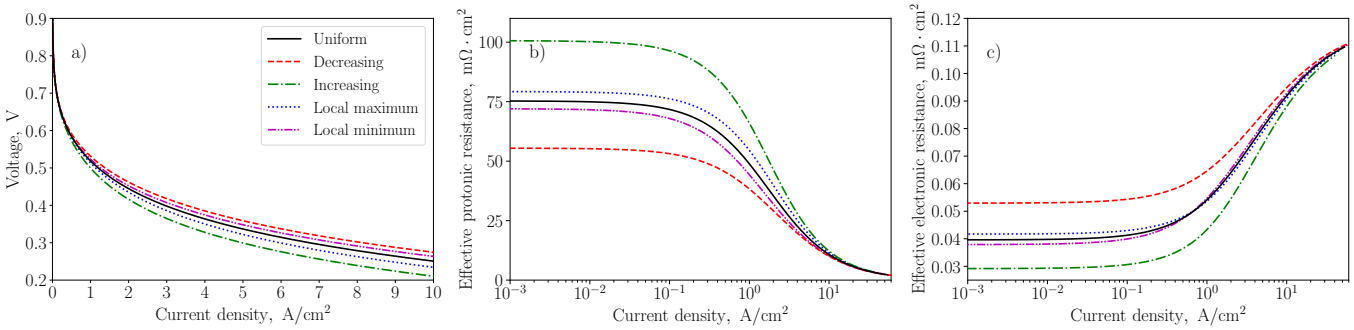

Figure S14: Comparison of the polarization curves (a) and ohmic resistances (b, c) of the catalyst layer simulated numerically for the active-area and double-layer capacitance distributions from Figure S13. The ohmic resistance was computed through ohmic heating (equations (6) and (7)).

5. Effect of heterogeneous active area and double-layer capacitance

The heterogeneous active-area and double-layer-capacitance distributions used in this work are provided in Figure S13. The corresponding polarization and resistance curves are shown in Figure S14. The H_2/O_2 spectra simulated at 1 A/cm^2 and the H_2/N_2 spectra are shown in Figures S15 and S16.

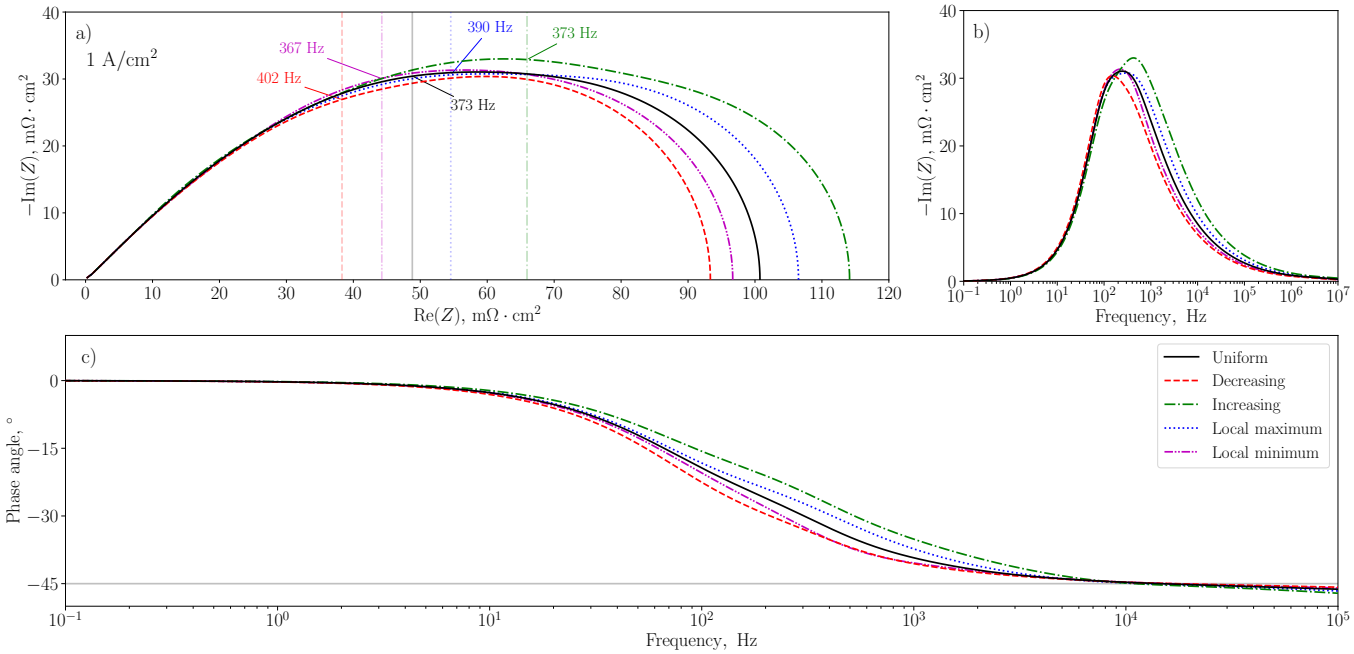

Figure S15: Comparison of the H_2/O_2 spectra simulated numerically for the active-area and double-layer capacitance distributions from Figure S13 at 1 A/cm^2: a) Nyquist plot and b) Bode plot of the imaginary impedance component. Vertical lines represent the total ohmic resistance computed through ohmic heating (equations (6) and (7)).

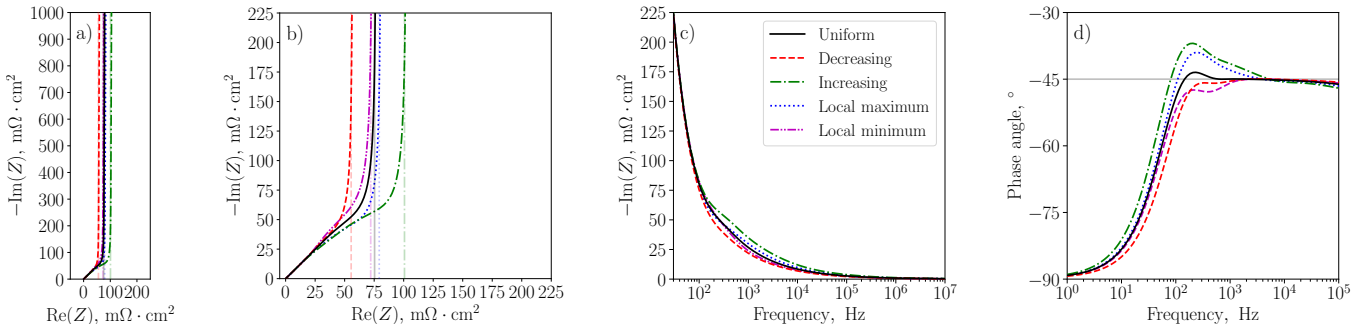

Figure S16: Comparison of the H_2/N_2 spectra simulated numerically for the active-area and double-layer capacitance distributions from Figure S13: a) Nyquist plot and b) Bode plot of the imaginary impedance component. Vertical lines represent the total ohmic resistance computed through ohmic heating (equations (6) and (7)).